Advanced Sustainable Photodetection: Systematic Fabrication and Analysis of Ag NPs/SWCNT/MWCNT Broadband Devices for Improved Environmental Monitoring

Taqwa Yaareb Yousif[1,*], Estabraq Abbas Abed[1], Asama N. Naje[2], Shahd Imad Hasan[1]

[1]*Department of Renewable Energy, Al- Karkh University of Science, Baghdad, Iraq*

[2]*Department of Physics, University of Baghdad, Baghdad, Iraq*

Abstract. This article elucidates a systematic fabrication and analysis procedure of Ag@SWCNT/MWCNT broadband photodetector via combined electrochemical and electro-explosion techniques. The microstructural, optical, electrical, and photoresponsive characteristics of the fabricated layers were thoroughly investigated. In detail, the optical spectra of the pronounced layers exhibited a wide-reaching absorption phenomenon along the scanned wavelength 200-800 nm. In conjunction, the fabricated devices demonstrated considerable photoresponsive parameters with higher photo-responsivity with Ag@SWCNT as compared to that using Ag@MWCNT. In detail, the addressed figure of merit delivers values of 3.3 and 0.17 A/W at wavelength of 365 nm, respectively. R_λ values of 3.9 and 4.2 A/W were obtained for the Ag@SWCNT photodetector under illumination wavelengths of 460 and 808 nm, respectively, indicating that such values were higher compared with the value at 365 nm wavelength. The external quantum efficiency (EQE) exhibited values of 11.09 and 0.53 at 365 nm for Ag@SWCNT and Ag@MWCNT, respectively.

Keywords: SWCNT; MWCNT; broadband, photodetector; Environmental Monitoring.

Corresponding *
Taqwa Yaareb Yousif
taqwa.yaareb@kus.edu.iq

1. Introduction

In recent times, porous silicon (PS) technologies have been well-thought-out as a potential pathway for functionality development of the bulk silicon-technology. Additionally, it has been recognized that bulk silicon personification is simple and cost-effective pathway for an advanced bulk silicon nanostructured characteristic, from which remarkably advanced behavior could be of reach. In this context, PS has drawn substantial reflection from industrial and research societies because of the well-oriented photoluminescence (PL) performance within ordinary laboratory conditions; the addressed singularity may range from violet to red spectrum as a function of the fabricated PS surface morphology, nanoparticle size, and crystal structure [1-3]. As such, PS technology is well-considered in multiple applications such as broad-band optoelectronics, through which UV-Vis-NIR incident wavelengths could be detected through signal conversion-based optoelectrical effect, have been widely explored. This is mainly due to wide-approaching applications in environmental monitoring, chemical/biological analysis, optical and space communications, etc. The most advanced broadband photodetectors available today are highly sought after for a variety of imaging, sensing, environmental monitoring, and communication applications. These include broad spectral photo-response, high sensitivity, room-temperature operation, and environmental stability. These days, sources that span a wide range of wavelengths, from ultraviolet to visible to near-infrared, offer significant and promising uses in environmental monitoring. For example, absorption spectroscopy in the near-infrared is one of the most crucial methods for gas detection in industrial and environmental monitoring. Additionally, one of the biggest threats to the ecosystem is the observation of an increase in ultraviolet (UV) radiation brought on by global warming [4, 5].

Particularly, there are two main optoelectrical effect pathways, photovoltaic and photo-conductive modes [6]. The former, usually, delivers suggestively high photo-response rate including homo/hetero junctions and Schottky contact. In contrast to the photovoltaic mode, the photoconductive mode demonstrates relatively high photocurrent gain due to multi-cycled carrier's singularity within the external circuit along with disadvantageous slow response/recovery proportion [7]. Hence, a countless research dedication is highlighted for the development of considerable photovoltaic mode optoelectronics; a number of nanostructures are, therefore, being considered for the addressed subject; for instance, Cadmium Oxide (CdO), Zinc oxide (ZnO), Tin oxide (SnO_2), copper oxide (CuO), Cadmium sulfide (CdS), and carbon nanotube multi-walled carbon nanotubes (MWCNT) and Single-walled carbon nanotubes (SWCNT)) [8-15]. Among these, CNTs, with their excellent durability, flexibility, and conductivity, exhibited a number of well-outlined applications in both optical and electrical solid-state nanodevices, photo-detector in particular [15]. Further, hybrid nanostructure-based CNTs are also being investigated in optoelectronic nanodevices through which broad-spectrum absorption is required [16]. For example, ZnO/CNTs structure demonstrated wide absorption range with considerable photoresponsive rate [17]. Another study reported MoS_2/CNTs heterostructure that covered both UV and Vis ranges of the spectrum [18].

In this attempt, this study aims to demonstrate the combination of Ag@CNTs/PS structure has a lot of potential for broadband wavelength multiplex detection of various analytes and environmental contaminants. In particular, Ag/CNTs/PS geometry is fabricated via combined electro-explosion and drop casting methods. Silver's combination of cost-effectiveness, excellent conductivity, unique catalytic properties, antimicrobial effects, strong SPR, and compatibility with nanostructured materials makes it a compelling choice for detector applications; while other metal such as platinum (Pt) and gold (Au) have their ad-vantages in terms of catalytic activity and stability. These factors contribute to its growing use in various sensing technologies, particularly where performance and economic feasibility are critical. The correlation between the structural, morphological, and optical characteristics along with the photo-responsive analysis are systematically illustrated.

2. Experimental procedure

2.1 Fabrication of porous Si layer

Porous Si wafer (p-type, $1-1.5\ \Omega.cm$, $508\pm10\ \mu m$) was attained via typical electrochemical etching framework. Systematically, 1 cm^2 p-type Si wafer was firstly cleaned using sonication solution consisting of distilled water and 48% HF (10:1) for 45 sec. Subsequently, the multi-cycled cleaned Si wafer was immersed in Teflon container that contains 1:1 (v/v) of EtOH and HF solution. Concurrently, 20 mA/cm^2 current was supplied for 10 minutes to the anode-based Si electrode with Pt serving as the cathode.

2.2 Synthesis of CNTs/Ag nanoparticles and fabrication of Ag@CNTs/PS photodetector

Ag nanoparticles were synthesized in distilled water through modified electro-explosion of wire approach in conjunction with 36 V DC battery [19]. In typical procedure, the negative potential was connected to a wire through which 100 A is passed to another ohmic contact. Herein, the resultant plasma-based 0.5 ml of Ag nanoparticles solution with the average diameter of 69.3 nm was thoroughly mixed with 2ml of SWCNT/MWCNT (95%, Nanostructured & Amorphous-Inc.). SWCNT was provided with 10-30 nm in diameter and 1-2 μm in length, while MWCNT has diameter and length of 1-2 nm and 30 µm, respectively. The final Ag-CNTs mixture was then deposited on the porous Si substrate through drop casting approach. In detail, the droplet made with volume of 30 µL, while the temperature was left as room temperature. Hereinafter, interdigital aluminum (Al) contacts were methodically deposited on the top of the casted layer via thermal evaporation technique with 500nm thickness as shown in Figure 1.

2.3 Characterizations

The structural features of the deposited layer/s were evaluated via X-ray diffraction (XRD, 2700 AB HAOYUAN) with CuKα radiation of 1.5406 A˙, while the morphological topographies were carried out using field emission scanning electron microscopy (MIRA3 TESCAN, FE-SEM). The optical characteristics were attained via UV-Vis spectroscopy (Shimadzu, UV-1800). The electrical properties were studied using Hall Effect measurements method (HMS-3000 Ecopia). Finally, the current-voltage (I-V) characteristics under both dark and multi-wavelengths monochromatic light source (365 nm, 460 nm, and 808 nm) emitting by laser diode with light intensity 5 mW/cm^2 focused over the light spot (1 cm^2) were recorded using source measure unit (SMU) Keithley 2401 in conjunction with PC-based Lab view software; the optical power was measured using optical power meter (Thorlabs) at room temperature, while the bias voltage applied for figure of merit evaluation was 5 V. The measured values of the attained current were repeated 5 time after which the average values were demonstrated for error analysis. The measurement setup is illustrated in Figure 1.

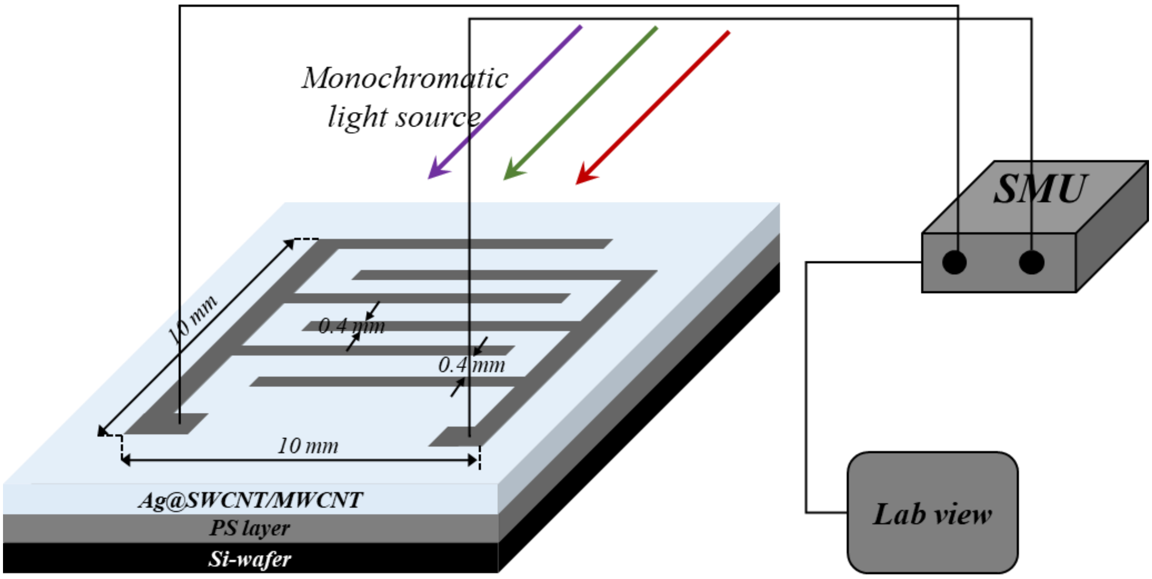

Figure 1. Schematic illustration of the fabricated photodetector along the measurement setup.

3. Results and discussion

The XRD patterns of the deposited nanostructured, namely: Ag, SWCNTs/Ag, and MWCNTs/Ag, are presented in Figure 2 (a-c). In detail, prominent peaks perceived at around 2θ ≈ 38.1°, 44.3°, 64.6°, 77.5° which are corresponded to (111), (200), (220), and (311) plans, respectively, indicate the occurrence of face center cubic Ag metallic particles; the attained XRD peaks (Figure 2, a) are indexed to the JCPDS data report no. 04-0783. Continuously, two main peaks (Figure 2, b & c) attained at 2θ ≈ 26.2° (002) corresponded to the formation of CNT (MWCNTs & SWCNTs) and 2θ ≈ 44.2° correspond to both of the miller indices (100) for CNT and (200) for Ag NPs; the former is corresponded to the CNT while the latter is indexed to Ag metallic particles. The occurrence of such Ag@MWCNTs/SWCNTs arrangement were found to be in good agreement with previously published reports [20].

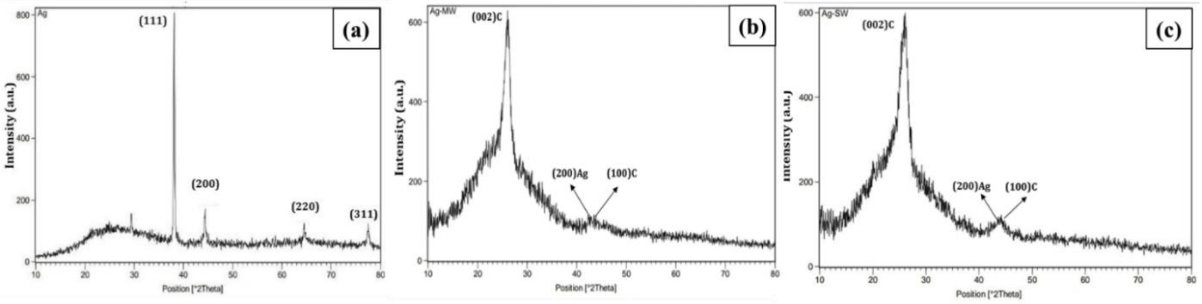

Figure 2. XRD patterns of the fabricated layers (a)Ag, (b)MWCNTs/Ag, and (c) SWCNTs/Ag.

The topographies of the fabricated layer/s are depicted in Figure 3 (a-d) through which it can be clearly observed that the attained porous Si layer (Figure 3, a) is highly uniformed along clear spikes formation; the addressed layer exhibited surface roughness and average diameter of 2.83nm and 81.35 nm, respectively. The attained Ag nanoparticles exhibited a compact surface topography along with average nanoparticles diameter of 69.3 nm (Figure 3, b). The surface morphology of the fabricated Ag@MWCNTs/SWCNTs layers exhibited clear formation of homogeneously distributed Ag nanoparticles along nanotubes (light spots, inset into Figure 3 (c and d)).

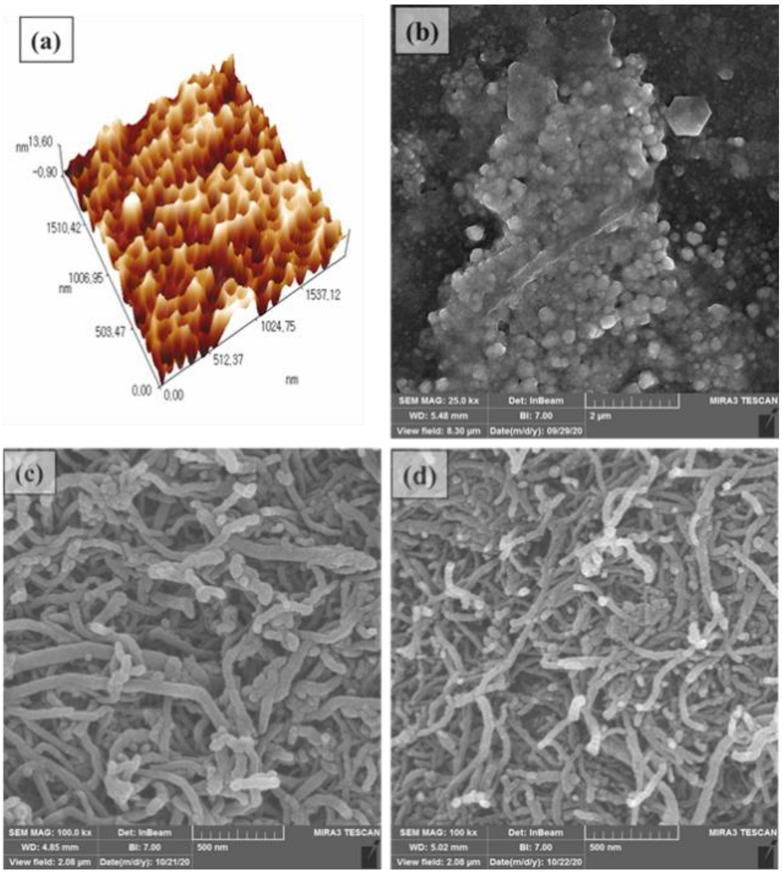

Figure 3. Surface topographies of (a) porous Si, (b) pure Ag, (c) Ag@MWCNTs, and (d) Ag@SWCNTs.

The UV-Vis spectra of the deposited layer/s are presented in Figure 4 (a-c) in which single Ag layer demonstrated rather wide absorption spectrum (Figure 4, a) along a distinguished broad resonance absorption peak at around 415 nm. The attained surface plasmon resonance (SPR) singularity was found to be continued along the visible spectrum in which previous published reports agreed with the proposed one [21]. The MWCNTs demonstrated a concentrated absorption peak at around 250 nm, while SWCNTs exhibited a distinctive absorption peak at 220 nm with a continuous absorption throughout the UV region (Figure 4, b). Continuously, the absorption spectra of Ag@MWCNT/SWCNT sample/s demonstrated relatively weak peaks for the pronounced samples (Figure 4, a and b) with overall absorption profile ranging from 200 to 800 nm. It could be clearly perceived that the attained peaks at around 415 is mainly attributed to the SPR characteristic within the Ag nanoparticles [22]. Additionally, a broad absorption behavior could be attained as a result of plasmon-plasmon interaction within the Ag nanoparticles geometry [23].

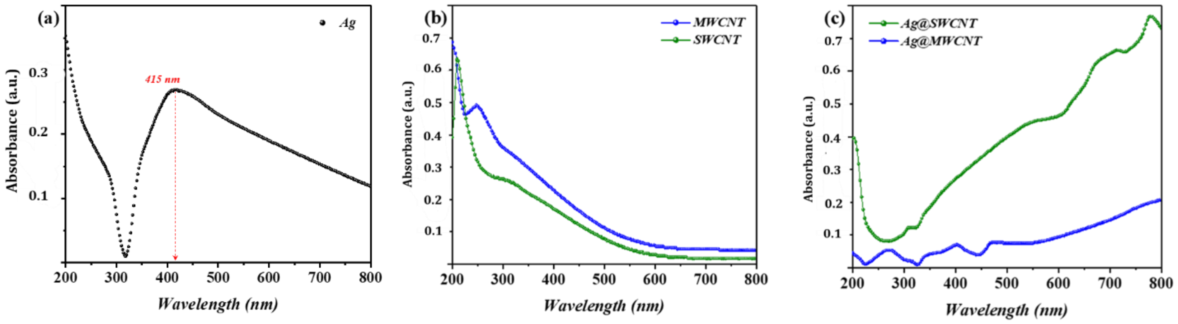

Figure 4. UV-Vis spectra of the deposited (a) Ag, (b) MWCNTs & SWCNTs, and (c) Ag@MWCNTs/SWCNTs.

Hall measurements have been done by Van der Pauw, model (HMS-3000 Ecopia). Measurements required four ohmic contacts on the sample (four Aluminum electrodes were deposited on its sides) with the applied magnetic field (0.551 T). Table 1 illustrates the measured Hall effect parameters of the fabricated layers in which it can be clearly perceived that SWCNT attained higher electrical parameters as compared to that attained for MWCNT; related to the structure of SWCNTs, which directly affects the electrical characteristics of nanotubes include their electrical nature, which can be either metallic or semiconducting dependence on the (n, m) index, which describes the chiral vector specifically, the angle between the lattices of graphite. In addition, the diameter of the SWCNT is shorter than that of MWCNT which in turn may results in higher conductivity of the attained geometry.

Table 1. Hall-effect characteristics of the deposited layers.

Parameter	SWCNTs/Ag NPs/PS	MWCNTs/Ag NPs/PS
Charge Concentration ($1/cm^3$)	-8.565×10^{19}	-5.260×10^{19}
Conductivity (1/ Ω.cm)	1.263×10^{3}	4.135×10^{2}
Mobility (cm^2/Vs)	9.204×10^{1}	4.907×10^{1}
Resistivity (Ω.cm)	7.918×10^{-4}	2.418×10^{-3}
Type	N-type	N-type

Figure 5 (a and b) elucidates the I-V characteristics of the fabricated Ag@MWCNTs/SWCNTs photodetectors considering a range of wavelengths, respectively. In general observation, the illuminated I-V profiles demonstrated higher current as compared to those obtained under the dark state. The stated dark current is occurred as a result of the adsorption of oxygen molecules according to $[O_2(g) + O_2^-(ad) \rightarrow O_2(g)]$. This particular observation could be highly traced because of an improved electron mobility in the Ag/SWCNT (Figure 5, b) as demonstrated in Hall effect analysis (Table 1). Continuously, the current acquired under illumination is mainly resulted from the energy of the incident photon/s which in turn demonstrated higher possibility of oxygen-adsorbed electron along photo-generated hole recombination $[h^+ + O_2^-(ad) \rightarrow O_2(g)]$ [24, 25]. Additionally, the I-V characteristics exhibited almost a linear increase as a function of the applied wavelength through which both proposed devices responded coherently to the applied wavelengths. In detail, higher I-V curve was attained within the IR region (808 nm) as compared to those obtained throughout the Vis and UV regions (460 and 365 nm, respectively). Such a behavior could be mainly attributed to the window effect via the utilized Si wafer of the fabricated device/s. High current obtained under visible region (465 nm) could be due to the presence of Ag nanoparticles within the proposed structure as demonstrated in UV-Vis analysis, while the current noticed under the illumination of 365 nm could be because of the existence of MWCNT/SWCNT within the fabricated photodetector; this was previously predicted from the UV-Vis analysis (Figure 4, a-c). It is worth mentioning that higher dark/illuminated current was attained with Ag@SWCNT photodetector as compared to that fabricated with MWCNT, with respect to the wavelength applied.

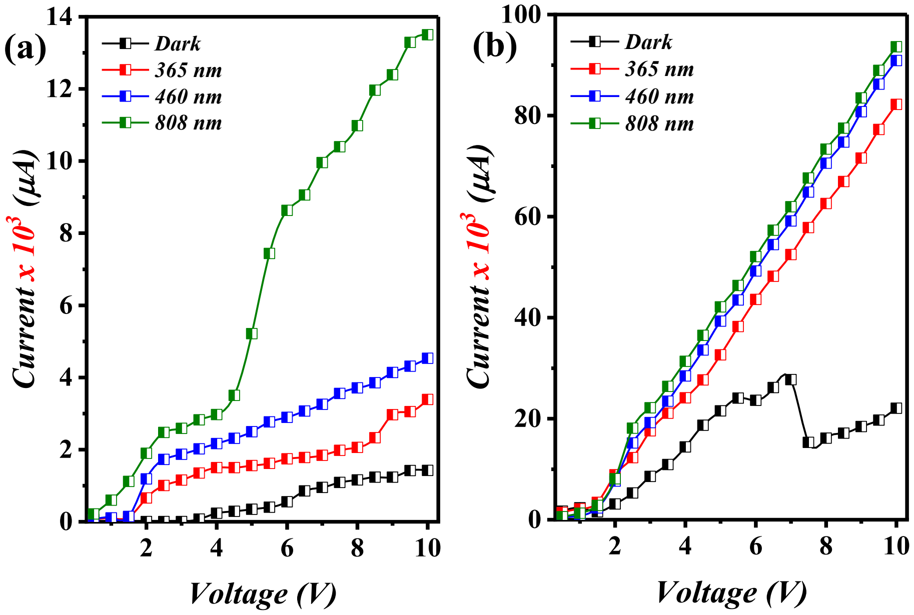

Figure 5. I-V characteristics of the fabricated (a) Ag@MWCNT and (b) Ag@SWCNT.

Figure 6 illustrates the attained current under dark as well as the utilized wavelength-based illumination (365, 460, and 808 nm). The depicted current is considered at 5 V, wherein 5 repeated measurements were considered and the average value is demonstrated accordingly. It can be clearly noticed that the measured values are not overlapped which in turn proves the accuracy of the measured current.

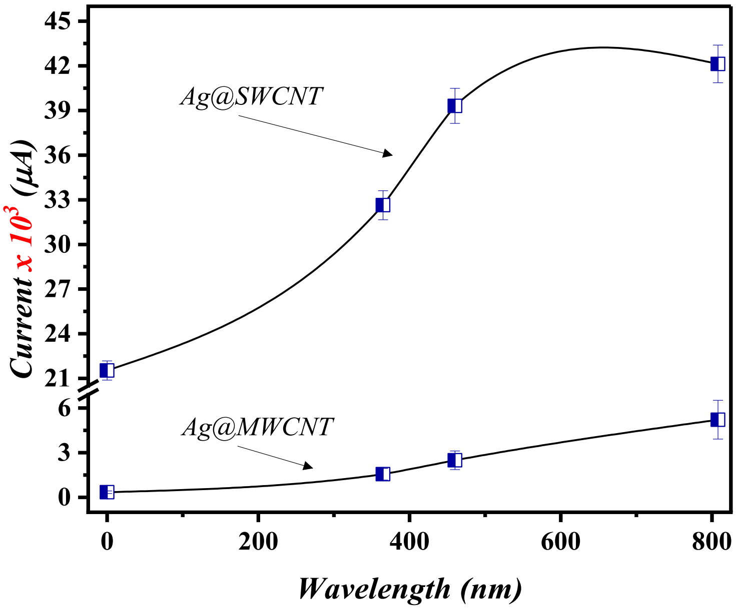

Figure 6. Variation between incoming wavelength and current generated in photodetector.

Further, the calculated figure-of-merits are depicted in Figure 7 (a and b) for Ag@SWCNT Ag@MWCNT photodetectors, respectively. Specifically, photo-responsivity ($R_\lambda = I_{ph}/P_{in}$) [26] demonstrated an increasing trend from 3.264 to 4.213 A/W, for Ag@SWCNT photodetector as the illumination wavelength increased semi-linearly from 365 to 808 nm (Figure 6, a); similar behavior was perceived for the photo-detectivity $[D^* = (I_{ph}/P_{in})/(2qI_D)^{1/2}]$ along the utilized wavelengths. However, the external quantum efficiency ($EQE = (I_{ph}/e)(P_i hv) \times 100\%$) [26] demonstrated an inverse profile which is attributed to the fact that the attained increment in the ratio of the photocurrent is lower than that of the applied wavelength. The photo to dark current ration, on the other hand, exhibited a considerable linear ratio increment as a function of wavelength with $R^2 = 0.851$, inset into Figure 7 (a). Continuously, the stated figure-of-merits of Ag@MWCNT photodetector delivered lower values (Figure 7, b) which in turn suggests preferable electron transfer mechanism in the utilized Ag@SWCNT photodetector as compared to that of Ag@MWCNT [27, 28]. Further, the linear correlation attained in Ag@SWCNT device was notivcebly enhanced as a function of the applied wavelength for the investigated Ag@MWCNT photodetector with an average R^2 of 0.969, inset into Figure 7 (b).

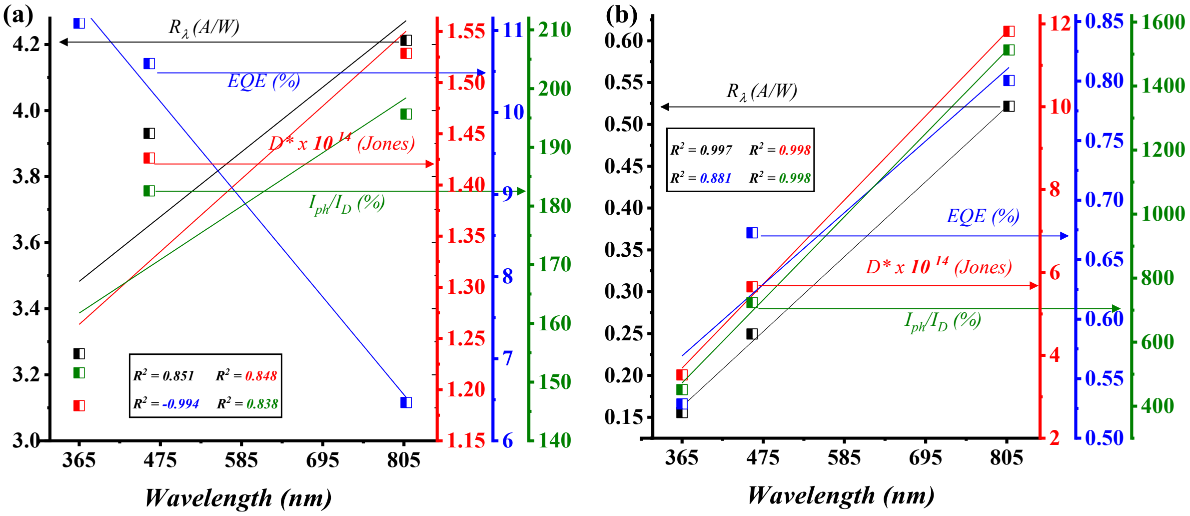

Figure 7. Figure of merits of the fabricated devices; (a) Ag@SWCNT and (b) Ag@MWCNT.

3. Conclusions

Nanostructured Ag@SWCNT and Ag@MWCNT wide range of spectral response photodetectors were successfully fabricated via electro-explosion wire method and direct mixing. The optical analysis exhibited a wide absorption range within the scanned spectrum. In conjunction, the fabricated devices related figure of merits exhibited linear increment (R^2~0.9) as a function of the utilized wavelength. In detail, the R_λ values were found to be 3.3, 3.9 and 4.2 A/W for wavelengths of 365, 460 and 808 nm for Ag@SWCNT based photodetector; these values were perceived to be relatively lower for device fabricated using MWCNT.

References

1. Kim, J., et al., *Near-ultraviolet-sensitive graphene/porous silicon photodetectors.* ACS applied materials & interfaces, 2014. **6**(23): p. 20880-20886.
2. Sanchez-Salcedo, R., P. Sharma, and N.H. Voelcker, *Advancements in porous silicon biosensors for point of care, wearable, and implantable applications.* ACS Applied Materials & Interfaces, 2025. **17**(2): p. 2814-2843.
3. Kang, R.H., et al., *Recent advances of macrostructural porous silicon for biomedical applications.* ACS applied materials & interfaces, 2025. **17**(4): p. 5609-5626.

4. Khdr, N.F., B.G. Rasheed, and B.M. Ahmed. *Optical and Morphological Properties of Silver Nanoparticles Synthesis by Q-Switched Nd-YAG Laser*. in *Materials Science Forum*. 2021. Trans Tech Publ.
5. Jaber, G.S., K.S. Khashan, and M.J. Abbas. *Study the characteristics optical and structure properties of ZnO-nanoparticles fabricated by laser ablation in liquid*. in *Journal of Physics: Conference Series*. 2021. IOP Publishing.
6. Ha, H.J., et al., *Real-time ultraviolet monitoring system with low-temperature solution-processed high-transparent p–n junction photodiode with a fast responsive and high rectification ratio.* ACS applied materials & interfaces, 2024. **16**(30): p. 40139-40148.
7. Anilkumar, V., et al., *Metal-Doped MAPbBr3 Single Crystal p-n Junction Photodiode for Self-Powered Photodetection.* Advanced Optical Materials, 2024. **12**(9): p. 2302032.
8. Sharaf, H.K., N.F. Khdr, and J.S. Chiad, *Characterization of the laminated carbon fiber with perlon layers for prosthetic socket applications: Numerical and experimental analysis.* Next Materials, 2025. **9**: p. 101096.
9. Raheema, M.H. and G.S. Jaber, *Synthesis of Carbon Nanotubes Using Modified Hummers Method for Cathode Electrodes in Dye-Sensitized Solar Cell.* Baghdad Science Journal, 2023. **20**(6).
10. Ismail, R.A., et al., *Preparation and characterization of carbon nanotubes by pulsed laser ablation in water for optoelectronic application.* Physica E: Low-dimensional Systems and Nanostructures, 2020. **119**: p. 113997.
11. Abd, A.N., R.A. Ismail, and N.F. Habubi, *Characterization of CdS nanoparticles prepared by laser ablation in methanol.* Journal of Materials Science: Materials in Electronics, 2015. **26**(12): p. 9853-9858.
12. Kumar, M., et al., *High-performance self-powered UV photodetectors using SnO2 thin film by reactive magnetron sputtering.* Sensors and Actuators A: Physical, 2024. **373**: p. 115441.
13. Kumar, A., S. Sahu, and M. Bhattacharjee, *Ultrafast Self-Powered Copper Oxide Composite-Based Vis-NIR Photodetector Probe.* ACS Applied Electronic Materials, 2024. **6**(9): p. 6457-6465.
14. Manikandan, V., et al., *Solution-processed UV–visible photodetector based on Ag enfold g-C3N4 nanosheets with MWCNT nanotube hybrid nanostructure.* Optical Materials, 2022. **134**: p. 113086.
15. Capista, D., et al., *SWCNT-Si photodetector with voltage-dependent active surface.* Nano Express, 2023. **5**(1): p. 015004.

16. Pelella, A., et al., *A self-powered CNT–Si photodetector with tuneable photocurrent.* Advanced Electronic Materials, 2023. **9**(1): p. 2200919.
17. Ibrahim, M.W., et al., *Photocatalytic degradation of pharmaceutical pollutants using zinc oxide supported by mesoporous silica.* Journal of Sol-Gel Science and Technology, 2021. **98**(2): p. 300-309.
18. Wang, Q., et al., *Preparation and bolometric responses of MoS2 nanoflowers and multi-walled carbon nanotube composite network.* Nanomaterials, 2022. **12**(3): p. 495.
19. Sen, P., et al., *Preparation of Cu, Ag, Fe and Al nanoparticles by the exploding wire technique.* Journal of Chemical Sciences, 2003. **115**(5): p. 499-508.
20. Cai, X., S. Wang, and L.-M. Peng, *Recent progress of photodetector based on carbon nanotube film and application in optoelectronic integration.* Nano Res. Energy, 2023. **2**(2): p. e9120058.
21. Amirjani, A. and D.F. Haghshenas, *Ag nanostructures as the surface plasmon resonance (SPR)-based sensors: a mechanistic study with an emphasis on heavy metallic ions detection.* Sensors and Actuators B: Chemical, 2018. **273**: p. 1768-1779.
22. Shimizu, K.-i., et al., *Formation and redispersion of silver clusters in Ag-MFI zeolite as investigated by time-resolved QXAFS and UV− Vis.* The Journal of Physical Chemistry C, 2007. **111**(4): p. 1683-1688.
23. Mbhele, Z., et al., *Fabrication and characterization of silver− polyvinyl alcohol nanocomposites.* Chemistry of Materials, 2003. **15**(26): p. 5019-5024.
24. Jaber, G.S., et al., *Improving the glass ionomer restoration by Incorporating strontium NPs coated with AuNPs manufactured by laser ablation in liquid.* Inorganic Chemistry Communications, 2024. **164**: p. 112411.
25. Wang, Z., et al., *Transferable and flexible nanorod-assembled TiO2 cloths for dye-sensitized solar cells, photodetectors, and photocatalysts.* ACS nano, 2011. **5**(10): p. 8412-8419.
26. Huang, Z., et al., *Integration of photovoltaic and photogating effects in a WSe 2/WS 2/p-Si dual junction photodetector featuring high-sensitivity and fast-response.* Nanoscale Advances, 2023. **5**(3): p. 675-684.
27. Bao, W., et al., *Tunneling resistance and its effect on the electrical conductivity of carbon nanotube nanocomposites.* Journal of Applied Physics, 2012. **111**(9).
28. Zhang, X., et al., *Understanding the mechanical and conductive properties of carbon nanotube fibers for smart electronics.* Advanced Materials, 2020. **32**(5): p. 1902028.